A MODEL-BASED APPROACH TO THE COMMON-DIFFRACTION-SURFACE STACK - THEORY AND SYNTHETIC CASE STUDY

HASHEM SHAHSAVANI[1], JÜRGEN MANN[2], IRADJ PIRUZ[1] and PETER HUBRAL[2]

1 Faculty of Mining, Petroleum and Geophysics, Shahrood University of Technology, Shahrood, Iran.
2 Geophysical Institute, Karlsruhe Institute of Technology, Hertzstr. 16, 76187 Karlsruhe, Germany.

(Received March 8, 2011; revised version accepted July 4, 2011)

ABSTRACT

Shahsavani, H., Mann, J., Piruz, I. and Hubral, P., 2011. A model-based approach to the Common-Diffraction-Surface stack - theory and synthetic case study. *Journal of Seismic Exploration*, 20: 289-308.

The Common-Reflection-Surface stack method parameterizes and stacks seismic reflection events in a generalized stacking velocity analysis. The common 2D implementation of the Common-Reflection-Surface stack is able to consider a discrete number of events contributing to a given stack sample such that conflicting dip situations can be handled. However, the reliable detection of such conflicting dip situations is difficult and missed contributions to the stacked section might cause artifacts in a subsequent poststack migration, just as unwanted spurious events that might be introduced by this approach. This is deleterious for complex data where prestack migration is no viable option due to its requirements concerning the accuracy of the velocity model. There, we might have to rely on poststack migration, at least for the first structural image in the depth domain. In addition to the approach which considers a small number of discrete dips, the conflicting dip problem has been addressed by explicitly considering a virtually continuous range of dips with a simplified Common-Reflection-Surface stack operator. Due to its relation to diffraction events, this process was termed Common-Diffraction-Surface stack. In analogy to the Common-Reflection-Surface stack, the Common-Diffraction-Surface stack has been implemented and successfully applied in a data-driven manner. The conflicting dip problem has been fully resolved in this way, but the approach comes along with significant computational costs. To overcome this drawback we now present a much more efficient model-based approach to the Common-Diffraction-Surface stack which is designed to generate complete stack sections optimized for poststack migration. Being a time-domain stacking process, this approach only requires a smooth macro-velocity model of minor accuracy. We present the result for the Sigsbee 2A data set and compare its poststack-migrated result to its counterparts obtained with the data-driven Common-Diffraction-Surface approach or the Common-Reflection-Surface stack, respectively. Compared to the data-driven approach, the computational effort is dramatically reduced with even improved results very close to the results of a prestack depth migration.

KEY WORDS: common-reflection-surface stack, conflicting dips, wavefield attributes, dip moveout operator, ray tracing.

0963-0651/11/$5.00

INTRODUCTION

The Common-Reflection-Surface (CRS) stack method has been extensively discussed in various publications during the last decade. In the following, we will therefore restrict the discussion of the CRS method to its very basic essentials required in the scope of this paper. The CRS method follows the concepts of the classical stacking velocity analysis, i.e., the local parameterization and stacking of reflection events by means of an analytic second-order approximation of the reflection traveltime, and the determination of the stacking parameters by means of coherence analysis (see, e.g., Mann et al., 1999; Jäger et al., 2001). Conventional stacking velocity analysis is applied within individual common-midpoint gathers with the stacking velocity as the only stacking parameter (in general azimuth-dependent in 3D) and often on a relatively coarse grid, only. In contrast, the CRS approach is applied on a fine grid and also takes neighboring common-midpoint gathers into account, acknowledging the fact that reflection events are caused by spatially contiguous reflector elements in depth. The same concepts are employed in similar imaging methods like multifocusing (see, e.g., Gelchinsky et al., 1999a,b; Landa et al., 1999, and various more recent publications).

The relation between conventional stacking velocity analysis and the CRS approach has, e.g., been described by Hertweck et al. (2007). To highlight the similarities between these approaches, they expressed the CRS operator in terms of horizontal slowness and two imaging velocities, one of the two latter representing the well-known stacking velocity. Equivalent formulations can be given in terms of spatial traveltime derivatives in terms of paraxial ray theory (Schleicher et al., 1993) or in terms of properties of hypothetical wavefronts (Tygel et al., 1997), namely the emergence direction of the normal ray connecting the reflection point to the surface and the curvatures of wavefronts associated with a point source at the reflection point or a exploding reflector segment around the latter, respectively. For the sake of consistence with related publications, we will use the latter description in the following, although traveltime derivatives will come into play as well.

In its simplest implementation, the CRS stack determines only one optimum stacking operator for each zero-offset (ZO) sample to be simulated. Along this optimum operator, we obtain the maximum coherence in the seismic reflection data. If there is only one reflection event contributing to the considered sample or no coherent event at all, this is sufficient. However, in the presence of curved reflectors, diffractors, or multiples various events might intersect each other and/or themselves, such that a single stacking operator per ZO sample is no longer sufficient to simulate a stacked section containing all relevant contributions. To account for such conflicting dip situations, Mann (2001, 2002) proposed to allow for a small, discrete number of multiple stacking operators for a particular ZO sample. The determination of additional stacking

parameters associated with local coherence maxima is quite simple, but the main difficulty in this approach is to identify conflicting dip situations and to decide how many contributions should actually be considered. This implies a tricky balancing between lacking contributions and potential artifacts due to the unwanted parameterization of spurious events. Due to the discrete number of considered events, the number of detected and, thus, imaged events might change from sample to sample such that seismic events might still show up fragmented.

The introduction of inversion methods fully exploiting the information contained in the CRS stacking parameters (Duveneck, 2004a,b) enabled a consistent imaging workflow consisting of CRS stack, normal-incidence-point (NIP) wave tomography, and prestack depth migration (see, e.g., Mann et al., 2003; Heilmann et al., 2004; Hertweck et al., 2004). In this workflow, the stacked section mainly serves as an intermediate result for automated picking rather than as a final image for interpretation. Thus, lacking contributions in the stacked section due to conflicting dip situations are acceptable and do not affect the final depth image. However, in data of complex nature and/or high noise level, generating a macro-velocity model of sufficient accuracy for prestack depth migration might not be feasible with reasonable effort. In such cases, poststack depth migration with its much lower requirements in terms of velocity model accuracy is more attractive - and the completeness of the stacked section turns into a relevant issue again.

To obtain a stack section containing all intersecting events, Soleimani et al. (2009a,b) proposed an adapted CRS strategy by merging concepts of the dip moveout correction (e.g., Hale, 1991) with the CRS approach: instead of only allowing a single stacking operator or a small discrete number of stacking operators per sample, a virtually continuous range of dips is considered. To simplify this process and to further emphasize usually weak diffraction events, this has been implemented with a CRS operator reduced to (hypothetical) diffraction events. This so-called Common-Diffraction-Surface (CDS) stack approach has been successfully applied to complex land data (Soleimani et al., 2010). However, the approach is quite time consuming, as separate stacking operators have to be determined for each stacked sample to be simulated and each considered dip in a data-driven manner by means of coherence analysis in the prestack data. In the following, we will refer to this approach as the data-driven CDS stack.

In this paper, we propose and apply a model-based approach to the CDS stack. We assume that a smooth macro-velocity model has already been determined, e.g., by means of a processing sequence consisting of CRS stack, automated smoothing and picking, and NIP-wave tomography. Of course, a macro-velocity model generated with any other inversion approach can be used as well. In such a smooth macro model, the parameters of the CDS stacking

operators can be easily forward-modeled by means of kinematic and dynamic ray tracing such that their determination by means of coherence analysis in the prestack is no longer required. In this way, a complete stacked section optimized for poststack depth migration can be generated in a much more efficient manner compared to the data-driven CDS approach.

TRAVELTIME APPROXIMATION

The CRS method is based on an analytical approximation of the reflection traveltime up to second order in terms of the half source/receiver offset h and the displacement of the source/receiver midpoint x_m with respect to the location x_0 of the stacked trace. This approximation can be expressed in different flavors, e.g., in a parametric form or in Taylor series expansions in terms of traveltime or squared traveltime, respectively (Höcht et al., 1999). The most popular form is the hyperbolic traveltime expansion, as it directly resembles the well-known common-midpoint traveltime approximation in the common-midpoint gather $x_m = x_0$. For the 2D case considered in this paper, the hyperbolic CRS traveltime approximation can be expressed as

$$t^2(x_m,h) = [t_0 + (2\sin\alpha/v_0)(x_m - x_0)]^2 + (2t_0\cos^2\alpha/v_0)[\{(x_m - x_0)^2/R_N\} + (h^2/R_{NIP})] \quad , \qquad (1)$$

with v_0 denoting the near-surface velocity. In this formulation, the latter is considered to be virtually constant and known within the applied stacking aperture. The stacking parameter α is the emergence angle of the normal ray, whereas R_N and R_{NIP} are the local radii of hypothetical wavefronts excited by an exploding reflector experiment or an exploding point source, respectively. Both hypothetical sources are attached to the (yet unknown) reflection point of the normal ray, the so-called NIP. All stacking parameters are defined at the acquisition surface (x_0;z = 0) and can be directly associated with traveltime derivatives in the prestack data.

For a true diffractor in the subsurface, an exploding point source experiment and an exploding reflector experiment obviously coincide such that $R_{NIP} \equiv R_N$. Thus, for *diffraction* events, the CRS traveltime eq. (1) reduces to the CDS traveltime approximation

$$t^2(x_m,h) = [t_0 + (2\sin\alpha/v_0)(x_m - x_0)]^2 + (2t_0\cos^2\alpha/v_0R_{CDS})[(x_m - x_0)^2 + h^2] \quad , \qquad (2)$$

with $R_{CDS} \equiv R_{NIP} \equiv R_N$. For *reflection* events, the CDS operator (2) is an inferior approximation compared to the full CRS operator (1) as $R_{NIP} \neq R_N$ if

the curvature of the reflector is not too large (a diffractor can be seen as a reflector with infinite curvature). Nevertheless, eq. (2) still allows to approximate the event within a reasonably chosen aperture which will be discussed below. For the data-driven CDS stack, this simplified operator has been chosen for performance reasons. For the model-based CDS stack, this simplification is mandatory, as there is no structural information on reflector curvatures contained in the considered smooth macro-velocity model. Thus, a forward-modeling of the parameter R_N is not possible anyway.

Note that the meaning of R_{CDS} depends on the way this stacking parameter is determined: in the forward-modeling discussed below, it is a completely local second-order property $R_{NIP,mod}$ of the emerging NIP wavefront at the considered ZO location x_0. In the CRS stack, the second-order property $R_{NIP,data}$ is determined from the prestack data within a finite aperture. Thus, $R_{NIP,data}$ is, in general, subject to spread length bias and does not exactly coincide with the forward-modeled $R_{NIP,mod}$ (see, e.g., Müller, 2006). In the data-based CDS stack, R_{CDS} is influenced by both data-derived attributes $R_{NIP,data}$ and $R_{N,data}$. It represents a kind of weighted average of these both attributes, depending on the aspect ratio of the used aperture. In the context of this paper, we consider the forward-modeled case, i.e., $R_{CDS} \equiv R_{NIP,mod}$ which might differ significantly from the attribute obtained in the data-driven CDS approach. Finally, Garabito et al. (2001a,b) also used the CDS operator (2) for stacking. However, they applied it in a simultaneous two-parameter search for the combination of emergence angle α and the radius R_{CDS} yielding the highest coherence. Using only one operator per ZO sample, this data-driven approach does not address the conflicting dip problem considered here. Nevertheless, for the emergence angle associated with the highest coherence, it should resemble the stacking parameters of the data-driven CDS stack for the same angle.

FORWARD-MODELING

As mentioned above, the radius of the NIP wave is associated with a hypothetical point source at the NIP. The local curvature of the hypothetical wavefront triggered by such a point source is considered along the normal ray. The wavefront finally reaches the acquisition surface with the curvature $1/R_{NIP}$. Thus, the first step to model this parameter is to determine all potential normal rays by means of kinematic ray tracing. As we need these rays for given surface locations and emergence angles, the kinematic ray tracing is performed for the down-going rays.

Kinematic ray tracing consists in the calculation of the characteristics of the Eikonal equation

$$(\nabla T)^2 = 1/v^2(x,z) \quad , \tag{3}$$

which governs the kinematics of the wavefield in a 2D velocity field v(x,z). In the following, we will use the Einstein summation convention. According to Červený (2001), the Eikonal equation's characteristics

$$dx_i/du = d\mathcal{H}/dp_i,\ dp_i/du = -d\mathcal{H}/dx_i,\ dT/du = p_k(d\mathcal{H}/dp_k\ ;\ i = 1,2 \quad (4)$$

are defined in a generalized domain consisting of slowness vector **p** and spatial coordinates **x**. The projection of these characteristics into the space domain represents the searched-for ray paths. One possible form of the Hamiltonian is

$$\mathcal{H}(\mathbf{x},\mathbf{p}) = n^{-1}[(p_ip_i)^{n/2} - v^{-n}] = 0\ ;\ i = 1,2 \quad (5)$$

with n as a real number. Here, we will use the limit of $n \to 0$, which yields the Hamiltonian

$$\mathcal{H}(\mathbf{x},\mathbf{p}) = \tfrac{1}{2}\ln(p_ip_i) + \ln v = \tfrac{1}{2}\ln(v^2p_ip_i)\ . \quad (6)$$

For this case, the last characteristic in eq. (4) reduces to $dT/du \equiv 1$, i.e., the variable u along the ray is the traveltime. This directly allows to compute the ray tracing results on the required regular grid in ZO traveltime.

The corresponding kinematic ray tracing system, a system of four coupled ordinary differential equations, reads

$$dx_i/dT = (p_kp_k)^{-1}p_i,\ dp_i/dT = -\partial\ln v/\partial x_i\ ;\ i = 1,2 \quad (7)$$

and can be numerically integrated with the well known Runge-Kutta scheme of fourth order. The step length in the numerical solution is chosen as an integer fraction of the sampling rate of the stacked section to be simulated. In this way, we directly obtain the discrete points along the ray paths corresponding to the desired output locations in the ZO time domain.

The determination of R_{NIP} additionally requires dynamic ray tracing along the ray path. The derivation of the dynamic ray tracing system again starts with the Eikonal equation, now defined in ray-centered coordinates (s,n), with s being the coordinate tangent to the ray and n the coordinate normal to the ray. A Taylor expansion of the phase function T in the vicinity of the central ray introduces the second partial derivative M of the traveltime normal to the central ray (Červený, 2001):

$$M(u) = \partial^2T(u,n)/\partial n^2\big|_{n=0}\ . \quad (8)$$

The resulting ordinary differential equation of Ricatti type finally yields the dynamic ray tracing system consisting of two coupled ordinary differential equations of first order. For our chosen propagation variable $u \equiv t$ along the

central ray, this system reads

$$dq/dt = v^2 p, \quad dp/dt = -(1/v)(\partial^2 v/\partial n^2) q \quad , \tag{9}$$

which can be easily numerically integrated along the ray in parallel to the kinematic ray tracing described above. The properties p and q are related to different coordinate transforms, see Červený (2001) for details. The relevant property in our context is that their ratio coincides with the second traveltime derivative normal to the ray, eq. (8):

$$M(u) = p(u)/q(u) \quad . \tag{10}$$

In turn, for a point source at the NIP, $M(u_0)$ at the emergence point of the normal ray is directly related to the searched-for value of R_{CDS}:

$$1/R_{CDS} = v_0 M(u_0) = v_0[p(u_0)/q(u_0)] \quad , \tag{11}$$

with v_0 again representing the near-surface velocity at the emergence point.

A straightforward approach to this task is to integrate the dynamic ray tracing system upwards along the ray for a given point on the known down-going ray path with the according initial condition for a point source initial condition in the starting point, i.e., $q = 0$ and $p = 1$. However, this approach is highly inefficient for two reasons:

- dynamic ray tracing had to be performed separately for each considered point on the ray, i.e., hundreds or thousands of times along each ray,
- either the entire down-going ray paths had to be kept in memory, or kinematic ray tracing had to be repeated along the up-going ray paths again.

Instead, it is far more efficient to perform the dynamic ray tracing in parallel to the kinematic ray tracing along the down-going ray. However, in this way we cannot directly control the desired "initial" condition at the NIPs, because now the initial conditions are defined at the acquisition surface rather than at the NIPs. Fortunately, this problem can be addressed by solving the dynamic ray tracing system for two mutually orthogonal initial conditions, a point source and a plane wave at the initial point. The initial condition for the latter reads $q = 1$ and $p = 0$. Using the index 2 for the point source initial condition and index 1 for the plane wave initial condition, the solutions can be gathered in a ray propagator matrix $\mathbf{\Pi}$ (Červený, 2001):

$$\mathbf{\Pi}(u;u_0) = \begin{pmatrix} q_1 & q_2 \\ p_1 & p_2 \end{pmatrix} \quad , \tag{12}$$

which can be computed along the ray for any value of u along the ray with the two initial conditions being defined at the emergence location of the central ray associated with u_0. The ray propagator matrix $\mathbf{\Pi}(u;u_0)$ can be easily converted into the corresponding propagator matrix $\mathbf{\Pi}^b(u_0;u)$ describing the dynamic properties in opposite propagation direction along the ray:

$$\mathbf{\Pi}^b(u_0;u) = \begin{pmatrix} p_2 & q_2 \\ p_1 & q_1 \end{pmatrix} . \tag{13}$$

The first column of $\mathbf{\Pi}^b$ again corresponds to the plane wave initial conditions and the second column to the point source initial conditions, but these initial conditions are now defined at the considered point u on the central ray. As we compute $\mathbf{\Pi}$ along the down-going ray for all required locations u on the ray, $\mathbf{\Pi}^b$ is readily available, too. Its second column directly provides the searched-for solution of the dynamic ray tracing system at the emergence point of the central ray for a point source initial condition at any considered point u along the ray:

$$1/R_{CDS}(u) = v_0[q_1(u)/q_2(u)] . \tag{14}$$

IMPLEMENTATION ASPECTS

In addition to the stacked section, the CRS method provides sections with the maximum encountered coherence along the optimum CRS operators and their corresponding sets of wavefield attributes. In the model-based CDS approach we can also obtain similar sections with little additional effort. Although the stacking parameters do not have to be optimized as in the data-driven approaches, we can calculate the coherence along the individual CDS operators in the prestack data anyway. Note that this has to be performed only once per emergence angle for each ZO sample rather than dozens or hundreds of times as in the data-driven CDS stack. With the calculated coherence value, we can keep track of the CDS operator yielding the highest coherence for a particular ZO sample. In this way we can obtain a section of the highest encountered coherence, along with a section with the corresponding emergence angle α and a section with the corresponding radius of curvature R_{CDS}. Obviously, these resemble some of the CRS output sections and allow for a comparison with the CRS results, plausibility considerations etc.

In the data-driven stack approaches, the size of the search and stacking aperture in midpoint direction is often based on the size of the (estimated) projected first Fresnel zone. Furthermore, the aperture size has to be kept constant for a particular ZO sample as coherence measures are sensitive to the number of contributing traces which might deteriorate the coherence analysis (see, e.g., Mann, 2002). In the model-based approach, coherence analysis is not

employed, such that there is no need for a fixed aperture. In addition, the aperture size in midpoint direction has to be chosen smaller, as the CDS approximation with $R_{CDS} \equiv R_{NIP,mod}$ quickly deviates from the actual event in case of a reflection event. Therefore, we propose to use a smaller aperture centered around the so-called Common-Reflection-Point trajectory, where CRS operator and CDS operator are both tangent to the actual event. In a second order approximation, the Common-Reflection-Point trajectory describes the reflection response originating from a single reflection point with an inhomogeneous overburden. Its projection onto the acquisition surface reads (Höcht et al., 1999)

$$x_m(h) = x_0 + r_T\{\sqrt{[(h^2/r_T^2) + 1]} - 1\} \quad , \text{ with } r_T = R_{NIP}/2\sin\alpha \quad , \qquad (15)$$

and provides us with the lateral position of the center of the stacking aperture for each half-offset h. Obviously, all required properties in eq. (15) are readily available from the dynamic ray tracing. Along the Common-Reflection-Point trajectory, we can use comparatively small midpoint apertures and still ensure that we capture the contributions from the area of tangency between event and operator. With the width of the aperture, we can control to some extent whether diffraction events should be preferred against reflections events, as the CDS operator (2) fits diffraction events in a larger area of tangency.

SYNTHETIC EXAMPLE: SIGSBEE 2A DATA

To allow for a direct comparison with the data-driven CDS results by Soleimani et al. (2009a) we applied the model-based CDS approach to the well-known synthetic Sigsbee 2A data set (Pfaffenholz, 2001). This data set has been simulated by the SMAART JV by acoustic finite-difference modeling for the stratigraphic model shown in Fig. 1. Due to an absorbing top surface, the data contain no free-surface multiples. They consist of a total of 500 shot gathers with 150 ft shot interval and up to 348 receivers with a spacing of 75 ft. Temporal sampling rate is 8 ms, offsets range from 0 to 26025 ft.

As we want to focus on the stacking procedure rather than on the generation of the macro-velocity model by means of an inversion, we used the migration velocity model (not shown) distributed with the data as basis for our macro-velocity model. Due to the homogeneous water layer, the assumption of a virtually constant near-surface velocity in eqs. (1) and (2) is fully satisfied. The migration velocity model consists of the water column, the salt body, and a smooth background velocity, namely a constant vertical gradient of 0.3/s starting with 5000 ft/s at the seafloor. To obtain our macromodel, we first restored the seafloor at those locations where the salt body is in direct contact with the water column and then replaced the salt body by the background gradient. Finally, we smoothed the slowness in the velocity model five times

with the auto-convolution of a rectangular box of 525 × 525 ft² to get rid of the sharp velocity contrast at the seafloor without impairing the kinematics of the model.

The kinematic and dynamic ray tracing has been performed for each common midpoint bin, i.e., with a lateral spacing of 37.5 ft and a temporal step length of 0.8 ms. We did not allow turning rays, although this is supported by the implementation. Rays have been shot for an angle range of ±50° at 2° spacing. For the actual stacking process, the stacking parameter R_{CDS} is linearly interpolated in between the rays on a grid with 1° spacing. The midpoint aperture has a constant half-width of 300 ft centered around the approximate Common-Reflection-Point trajectory (15), the offset aperture ranges from 6000 ft at 2.3 s to 25000 ft at 11 s ZO traveltime. Semblance has been calculated within a time window of 56 ms.

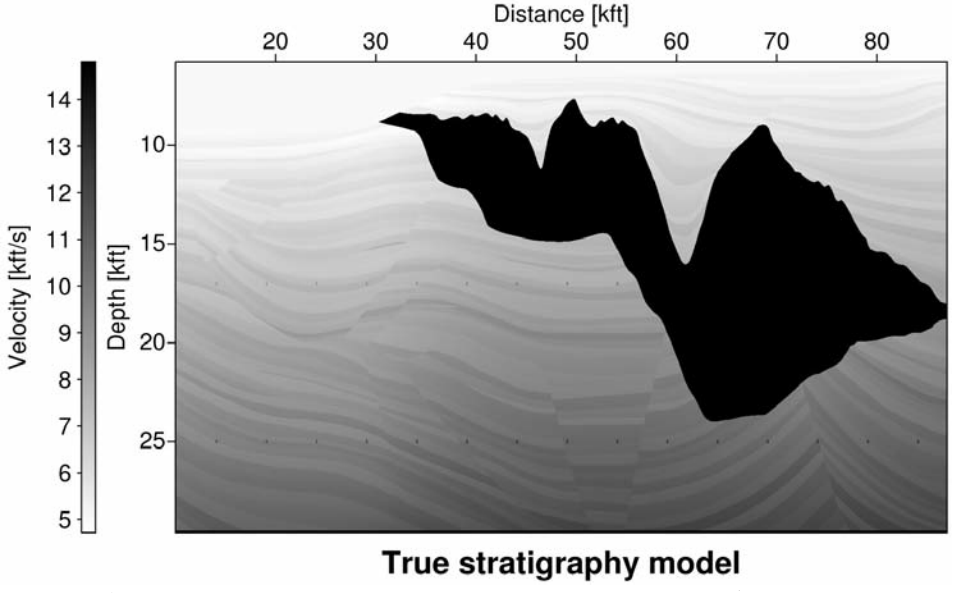

Fig. 1. Stratigraphic model used for the simulation of the Sigsbee 2A data.

The stacked section shown in Fig. 2 is very similar to the corresponding result obtained with its data-driven counterpart presented by Soleimani et al. (2009a) (not shown). The latter contains some spurious events which do not show up in the model-based result, but the main difference is the computational cost which is now more than two orders of magnitude lower for this data set

(not including the fact that the data driven result excludes the subsalt region for performance reasons). Of course, with the inherent second-order approximation of the CRS and CDS approaches, we cannot expect any reasonable result for the subsalt region, that is why we have removed the salt body in the macro-velocity model.

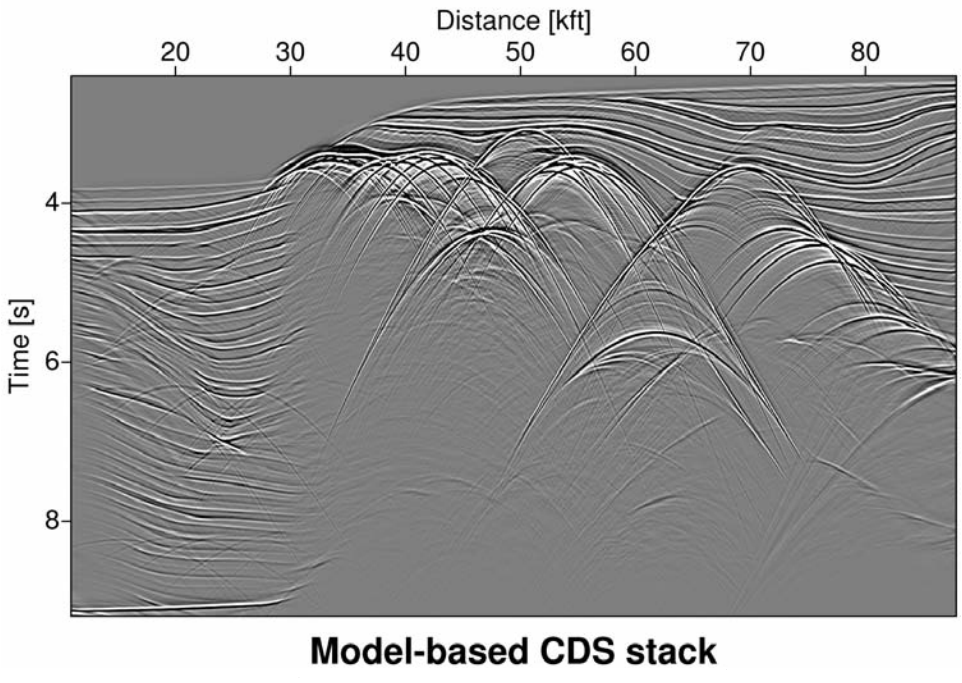

Fig. 2. Stacked section obtained with the model-based CDS approach. Note the various diffraction patterns caused by true diffractors, wedges, and model discretization.

The benefits of the complete handling of conflicting dip situations are best seen after a subsequent poststack migration using the macro-velocity model depicted in Fig. 1: Fig. 3 shows the result of a Kirchhoff poststack depth migration obtained for the model-based stack section shown in Fig. 2. All faults and diffractors are well focused, everything left of and above the salt is well imaged.

For comparison, we first revisited the CRS results by Mann (2002). They have been computed with two strategies: the simple approach considering only one dip per ZO sample and the extended approach with up to three dips per ZO sample. The poststack migration of the latter is depicted in Fig. 4. Faults and

diffractors are only partly focused. Spurious events in the stacked section, e.g., associated with a change of the number of contributions from sample to sample, cause various artifacts showing up as isochrones in the migrated section. The result based on the CRS stack with only one dip (not displayed) differs from the multi-dip CRS-stacked section in two respects: on the one hand, due to the lacking contributions at conflicting dip locations, the diffractors and faults appear even less focused and with lower amplitudes. On the other hand, the stacked section contains less spurious events such that we have less artifacts in the migrated section. In both cases, the results of poststack migration are unsatisfactory. The synclines in the top salt are incomplete and accompanied by coherent artifacts at slightly larger depths. As discussed by Mann (2002), the CRS stack has most likely also parameterized and stacked events associated with prismatic waves which lead to additional events in the stacked section. CRS for ZO simulation as well as poststack migration both imply normal rays, such that prismatic waves cannot be correctly imaged. Note that this effect hardly occurs in the model-based result shown in Fig. 3: As we explicitly forward-model normal rays there, the events from prismatic waves are attenuated by destructive interference.

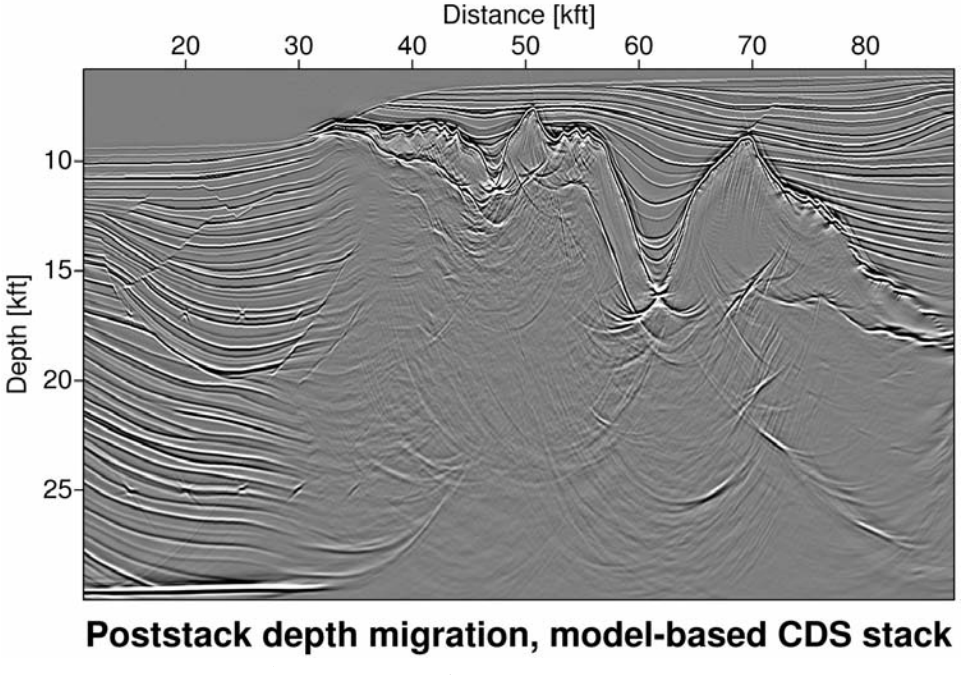

Fig. 3. Poststack Kirchhoff depth migration result for the model-based stack section shown in Fig. 2. Faults and diffractors are clearly focused.

For the next comparison, we revisited the data-driven CDS results by Soleimani et al. (2009a). The corresponding poststack-migrated section displayed in Fig. 5 shows well focused diffractors and faults and much less artifacts caused by spurious events compared to the CRS-based result in Fig. 4. As in the CRS-based result, the synclines in the top salt are still not properly imaged, as the data-driven CDS stack picks up prismatic waves as well. Note that the lower right part of the stacked section has not been computed for performance reasons such that this area remains either empty or shows some isochrones in the migrated section.

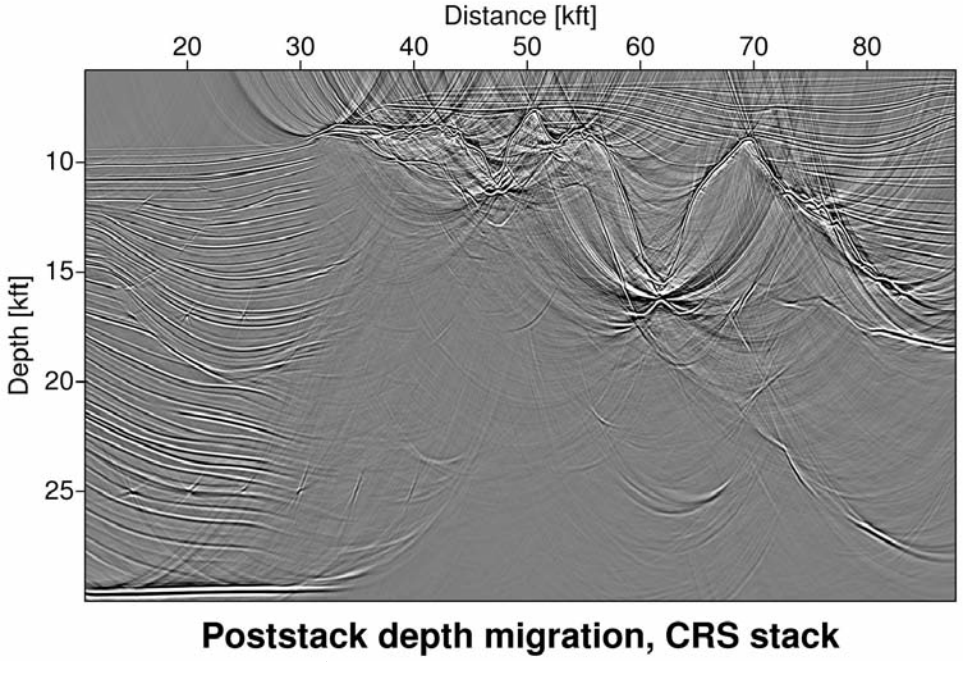

Fig. 4. Poststack Kirchhoff depth migration result for the CRS stack result published by Mann (2002). Up to three dips have been considered for each ZO sample. Faults and diffractors are only partly focused, many isochrones caused by spurious events can be seen.

As a final reference, we also applied a Kirchhoff prestack depth migration to the prestack data using the same macro-velocity model. The offset range and the muting of the migrated images gather were chosen such that they match the corresponding parameters used during the CDS stack as closely as possible. Fig. 6 shows the stack of about 80 offset bins with a width of 300 ft each after depth-dependent muting. The prismatic waves are again imaged wrongly, but

cancel out during the stack. This section is very similar to the poststack migration of the model-based CDS-stacked section in Fig. 2. Note that (of course, except for the subsalt part) the prestack migration has been performed with an optimum, i.e., kinematically perfectly correct velocity model. For less accurate models as usually achievable for real data, the prestack depth migration result will suffer much more from inaccuracy than the model-based CDS stack and the subsequent poststack migration.

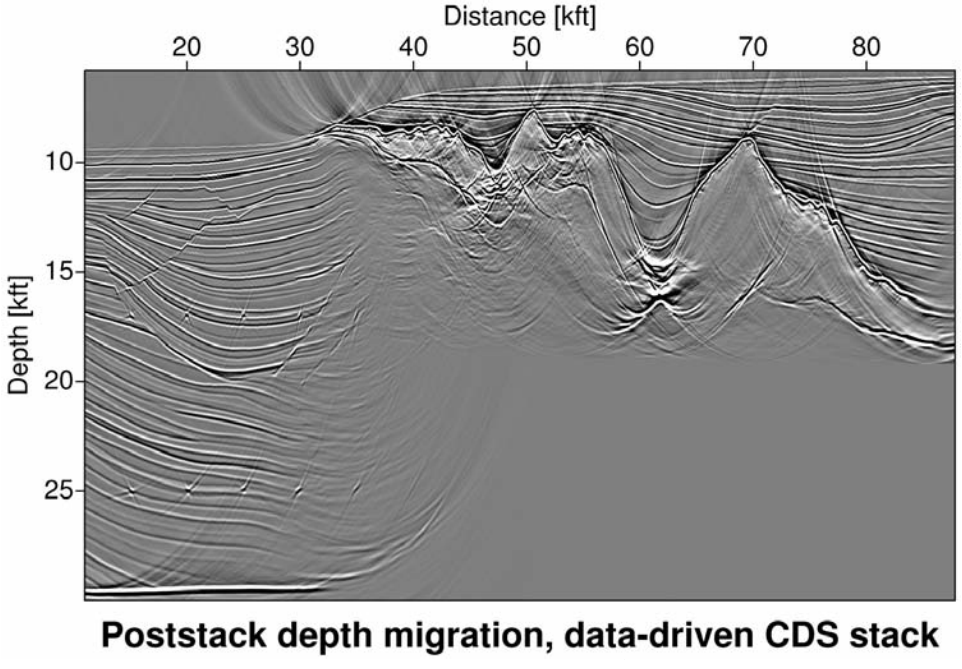

Fig. 5. Poststack Kirchhoff depth migration result for the data-driven CDS result published by Soleimani et al. (2009a). Faults and diffractors are well focused, there are only few isochrones caused by spurious events.

As mentioned above, we can perform coherence analysis along the individual forward-calculated stacking operators in the prestack data with little additional effort. In this way, we can obtain coherence and attribute sections resembling some of the corresponding sections known from the CRS stack approach: we simply keep track of the operator yielding the highest coherence measure for an individual ZO sample. As an example, the section with the highest coherence values encountered for each individual ZO sample is depicted Fig. 7. It allows to identify the reflection events and to evaluate the local fit

between CDS operator and event. As this section only shows the coherence for the most prominent events, less prominent events show up as local lowering of the coherence of the more prominent events they intersect. This behavior can, e.g., be seen along the diffraction events caused by the two horizontal rows of diffractors in the model.

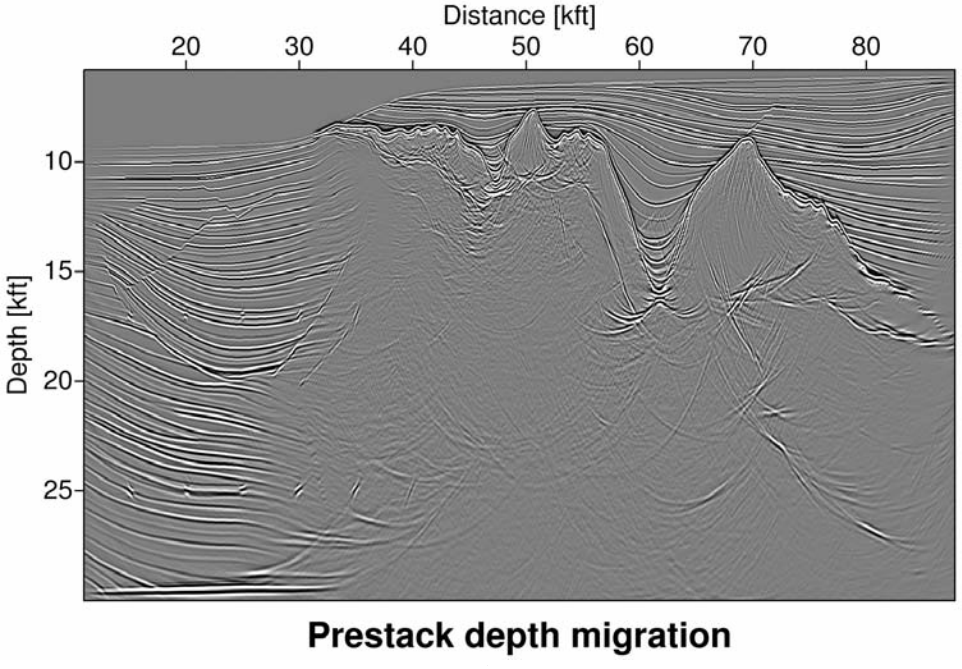

Fig. 6. Prestack Kirchhoff depth migration result with high similarity to the poststack result shown in Fig. 3. To allow for a fair comparison, the used offset range coincides with the one used for the CDS stack and the image gathers have been muted such that they mimic the time-dependent CDS stacking aperture in offset direction.

Together with the coherence along the most prominent operator, we can also store the corresponding stacking parameters α and R_{CDS} for each ZO sample. Due to the model-based calculation of R_{CDS}, these sections (not shown) look much smoother and more consistent than their CRS-based counterparts, almost without any outliers. At first glance, this appears to be useful for all applications using α and $R_{CDS} \equiv R_{NIP}$. One of them is inversion, either layer-based inversion (Majer, 2000; Majer et al., 2000), NIP wave inversion with a smooth model, or a combination of both (Müller, 2005, 2007). However, for inversion the attributes of the model-based CDS stack are obviously of no

use, because they are forward calculated. Inverting for them will, thus, at best reproduce the macro-velocity model already employed for stacking. In contrast, another application of these two attributes clearly benefits from their more stable and contiguous character: the attribute-based time migration introduced as a by-product of the CRS stack (Mann et al., 2000; Mann, 2002). This application is based on a point-to-point remapping of the stacked amplitude from the stationary point for ZO, i.e., the ZO image location, to the estimated apex of the time migration operator. Evidently, the latter estimation directly benefits from the higher stability of the attributes. In addition, this point-to-point migration can be performed separately for each emergence angle (not only for the most prominent one), such that the entire process turns into an operator-to-point migration much more similar to conventional poststack migration. Under such fortunate conditions, even this very simple approach yields striking results: Fig. 8 shows the result of this model-based time migration using the forward-modeled attributes on the fly. Although there are various artifacts in this section, the sedimentary part looks quite reasonable. Note that CRS-based

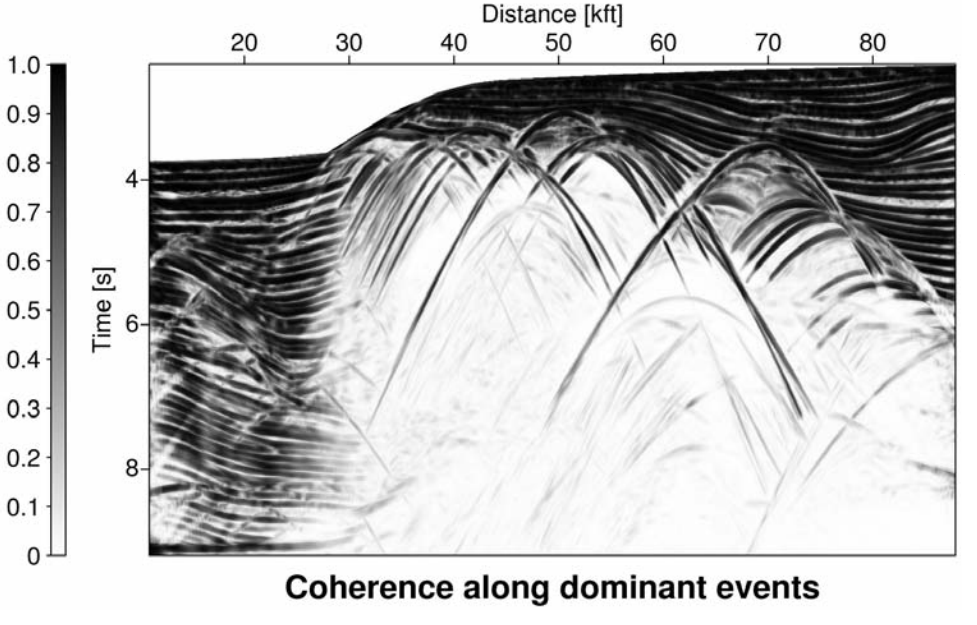

Fig. 7. Section of maximum encountered semblance corresponding to the stack section shown in Fig. 2. The associated attribute pairs (α,R_{NIP}) form attribute sections (not shown) resembling the analogous sections of the CRS approach.

counterpart (not shown) presented by Mann (2002) strongly suffers from high frequency noise and huge gaps in the events due to missing or unstable attributes, especially close to the top of the salt. Finally, we would like to mention that the data-driven CDS approach is not suited for this kind of migration, as it does not yield the required parameter R_{NIP}, see the section on traveltime approximation.

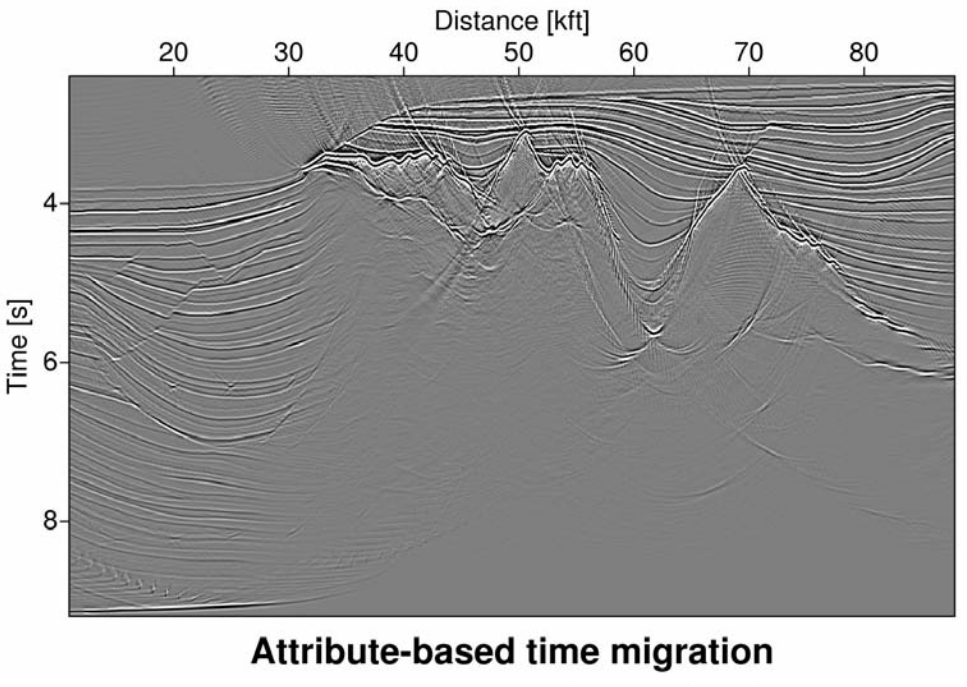

Fig. 8. Attribute-based time migration result obtained as a by-product of the model-based CDS stack. Compared to the CRS-based counterpart (not shown), more stable attributes and the quasi-continuous range of contributing emergence angles render this very simple approach feasible for the sedimentary regions.

CONCLUSIONS and OUTLOOK

We have implemented and applied a model-based approach to the common-diffraction-surface stack method. This method is intended to fully resolve the conflicting dip problem occurring in complex data and, thus, to allow to simulate a complete stacked section containing all mutually interfering reflection and/or diffraction events. In contrast to the entirely data-driven

common-diffraction-surface method (Soleimani et al., 2009a,b), this model-based approach is far more efficient. The required macro-velocity model can be generated with any inversion method, including the sequential application of common-reflection-surface stack and normal-incidence-point wave tomography. For the Sigsbee 2A data presented here, we excluded the inversion aspect and used a simplified version of the migration velocity model distributed with the data.

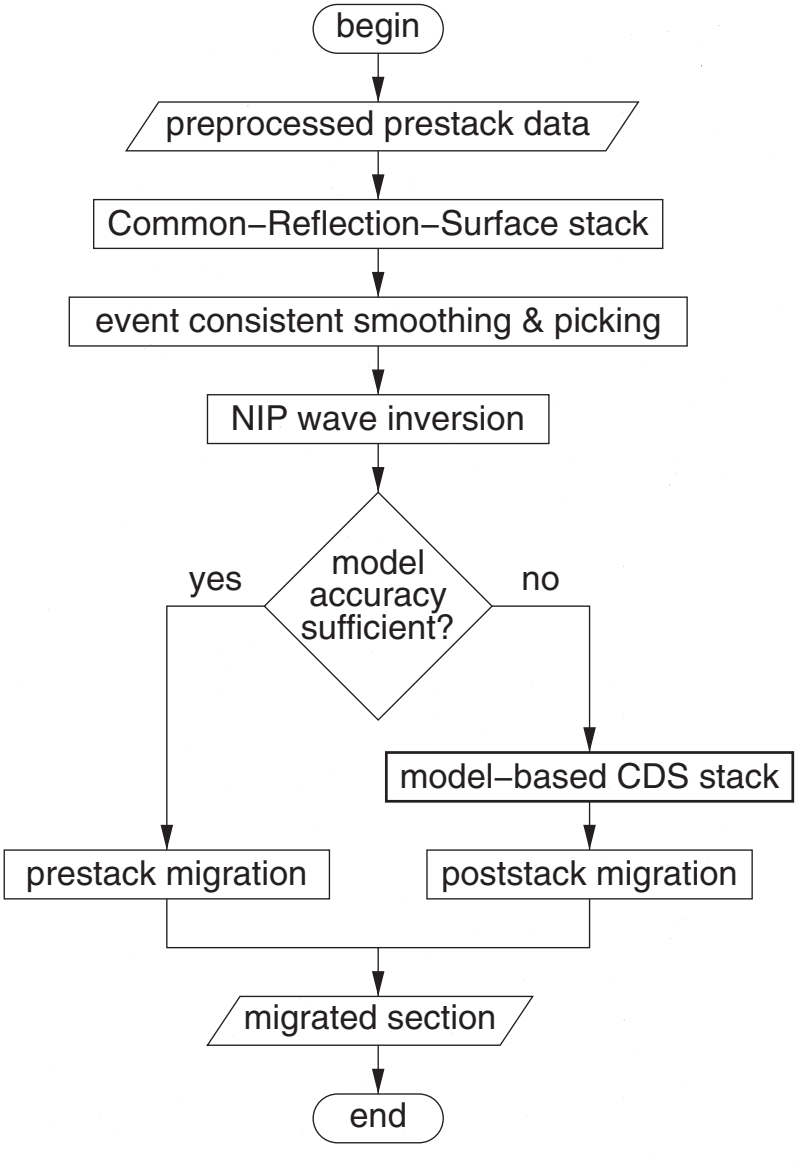

Fig. 9. Processing flowchart with an alternative to prestack migration using the model-based CDS stack plus poststack depth migration.

The model-based common-diffraction-surface stack is tailored to optimize the stacked section for a subsequent poststack depth migration. This is relevant for situations in which the generation of velocity models sufficiently accurate for prestack depth migration is difficult or even impossible. For the Sigsbee 2A data, we demonstrated that the model-based common-diffraction-surface stack allows to generate a poststack-migrated section very similar to the corresponding prestack migration result. The latter process usually requires a more accurate macro-velocity model. The new approach yields even better results than the data-driven approach in a significantly shorter computation time.

The model-based common-diffraction-surface stack can be integrated into the common-reflection-surface-based imaging workflow in situations where the result of normal-incidence-point wave tomography might not be sufficiently accurate to perform a prestack depth migration: as schematically shown in Fig. 9, prestack migration might be replaced by a sequence of model-based common-diffraction-surface stack and poststack migration. In this way, we can overcome the former deficiencies of the common-reflection-surface stack section which lead to gaps and artifacts in the poststack migration result.

ACKNOWLEDGMENTS

We would like to thank the sponsors of the Wave Inversion Technology (WIT) consortium and the Ministry of Science, Research and Technology, Iran, for their support. The Sigsbee 2A data have been provided by the Subsalt Multiple Attenuation And Reduction Technology Joint Venture (SMAART JV).

REFERENCES

Červený, V., 2001. Seismic ray theory. Cambridge University Press, Cambridge.

Duveneck, E., 2004a. 3D tomographic velocity model estimation with kinematic wavefield attributes. Geophys. Prosp., 52: 535-545.

Duveneck, E., 2004b. Velocity model estimation with data-derived wavefront attributes. Geophysics, 69: 265-274.

Garabito, G., Cruz, J.C., Hubral, P. and Costa, J., 2001a. Common reflection surface stack: A new parameter search strategy by global optimization. Expanded Abstr., 71st Ann. Internat. SEG Mtg., San Antonio: 2009-2012.

Garabito, G., Cruz, J.C.R., Hubral, P. and Costa, J., 2001b. Common reflection surface stack: a new parameter search strategy by global optimization. Ann. Report, Wave Inversion Technology Consortium, 4: 35-48.

Gelchinsky, B., Berkovitch, A. and Keydar, S., 1999a. Multifocusing homomorphic imaging - Part 1. Basic concepts and formulas. J. Appl. Geophys., 42: 229-242.

Gelchinsky, B., Berkovitch, A. and Keydar, S., 1999b. Multifocusing homomorphic imaging - Part 2. Multifold data set and multifocusing. J. Appl. Geophys., 42: 243-260.

Hale, D., 1991. Dip Moveout Processing. SEG, Tulsa, OK.

Heilmann, Z., Mann, J., Duveneck, E. and Hertweck, T., 2004. CRS-stack-based seismic reflection imaging - a real data example. Extended Abstr., 66th EAGE Conf., Paris: P211.

Hertweck, T., Jäger, C., Mann, J., Duveneck, E. and Heilmann, Z., 2004. A seismic reflection imaging workflow based on the Common-Reflection-Surface, CRS stack: theoretical background and case study. Expanded Abstr., 74th Ann. Internat. SEG Mtg., Denver: SP 4.3.

Hertweck, T., Schleicher, J. and Mann, J., 2007. Data-stacking beyond CMP. The Leading Edge, 26: 818-827.

Höcht, G., de Bazelaire, E., Majer, P. and Hubral, P., 1999. Seismics and optics: hyperbolae and curvatures. J. Appl. Geophys., 42: 261-281.

Jäger, R., Mann, J., Höcht, G. and Hubral, P., 2001. Common-Reflection-Surface stack: image and attributes. Geophysics, 66: 97-109.

Landa, E., Gurevich, B., Keydar, S. and Trachtman, P., 1999. Application of multifocusing method for subsurface imaging. J. Appl. Geophys., 42: 283-300.

Majer, P., 2000. Inversion of seismic parameters: determination of the 2-D iso-velocity layer model. M.Sc. thesis, University of Karlsruhe.

Majer, P., Höcht, G., Mann, J. and Vieth, K.-U., 2000. Inversion by means of kinematic wavefield attributes. Ann. Report, Wave Inversion Technology Consortium, 3: 39-49.

Mann, J., 2001. Common-Reflection-Surface stack and conflicting dips. Extended Abstr., 63rd EAGE Conf., Amsterdam: P077.

Mann, J., 2002. Extensions and Applications of the Common-Reflection-Surface Stack Method. Logos Verlag, Berlin.

Mann, J., Duveneck, E., Hertweck, T. and Jäger, C., 2003. A seismic reflection imaging workflow based on the Common-Reflection-Surface stack. J. Seismic Explor., 12: 283-295.

Mann, J., Hubral, P., Traub, B., Gerst, A. and Meyer, H., 2000. Macro-model independent approximative prestack time migration. Extended Abstr., 62nd EAGE Conf., Glasgow: B-52.

Mann, J., Jäger, R., Müller, T., Höcht, G. and Hubral, P., 1999. Common-Reflection-Surface stack - a real data example. J. Appl. Geophys., 42: 301-318.

Müller, N.-A., 2005. 3-D inversion with kinematic wavefield attributes. Extended Abstr., 67th EAGE Conf., Madrid: B040.

Müller, N.-A., 2006. Elimination of the spread-length bias in the Common-Reflection-Surface stack. Expanded Abstr., 76th Ann. Internat. SEG Mtg., Denver: 3006-3010.

Müller, N.-A., 2007. Determination of interval velocities by inversion of kinematic 3D wavefield attributes. Ph.D. thesis, Universität Karlsruhe.

Pfaffenholz, J., 2001. Sigsbee2 synthetic subsalt data set: image quality as function of migration algorithm and velocity model error. Workshop on velocity model independent imaging for complex media. Expanded Abstr., 71st Ann. Internat. SEG Mtg., San Antonio: W5-5.

Schleicher, J., Tygel, M. and Hubral, P., 1993. Parabolic and hyperbolic paraxial two-point traveltimes in 3D media. Geophys. Prosp., 41: 495-513.

Soleimani, M., Mann, J., Adibi Sedeh, E. and Piruz, I., 2010. Improving the seismic image quality in semi-complex structures in North East Iran by the CDS stack method. Extended Abstr., 72nd EAGE Conf., Barcelona: P398.

Soleimani, M., Piruz, I., Mann, J. and Hubral, P., 2009a. Common-Reflection-Surface stack: accounting for conflicting dip situations by considering all possible dips. J. Seismic Explor., 18: 271-288.

Soleimani, M., Piruz, I., Mann, J. and Hubral, P., 2009b. Solving the problem of conflicting dips in Common-Reflection-Surface stack. Extended Abstr., 1st Internat. EAGE Conf., Shiraz, Iran.

Tygel, M., Müller, T., Hubral, P. and Schleicher, J., 1997. Eigenwave based multiparameter traveltime expansions. Expanded Abstr., 67th Ann. Internat. SEG Mtg., Dallas: 1770-1773.